Ultrasonics 91 (2019) 34–44

Contents lists available at ScienceDirect

Ultrasonics

journal homepage: www.elsevier.com/locate/ultras

Numerical investigation of the effect of heterogeneity on the attenuation of shear waves in concrete

Aziz Asadollahi[a,*], Lev Khazanovich[b]

[a] University of Minnesota, Department of Civil, Environmental and Geo-Engineering, 500 Pillsbury Drive SE, Minneapolis, MN 55455, United States
[b] University of Pittsburgh, Department of Civil and Environmental Engineering, 3700 O'Hara Street, 742 Benedum Hall, Pittsburgh, PA 15261, United States

ARTICLE INFO

Keywords:
EFIT
Concrete
Attenuation
Shear waves
Scattering

ABSTRACT

Although ultrasonic transducers that emit horizontal shear waves are widely used in practice, no investigation has been conducted to study the attenuation of shear waves in concrete due to scattering by aggregates and air voids. Horizontal shear waves preserve more energy in comparison with longitudinal waves when propagating in concrete in low frequencies. However, the lower wavelength of shear waves increases the potential of their scattering attenuation in concrete. In this paper, we developed a 3D numerical tool and used it to study the scattering attenuation of horizontal shear waves in concrete in the 20–150 kHz frequency range. We showed that the scattering attenuation in this frequency range strongly depends on the size and material properties of aggregates. The shape of the aggregates and the presence of air voids slightly affected the scattering attenuation.

1. Introduction

Concrete has been one of the most used construction materials in the world, and monitoring the integrity of these structures is becoming more crucial due to the aging of the infrastructures made of this material. Nondestructive testing (NDT) allows the evaluation of the health of structures without causing any damage. Ultrasonic nondestructive testing allows the visualization of major discontinuities in acoustic impedance in deeper depths in the test specimens [1–3]. Therefore, they are appropriate for visualizing cracks, rebars and cavities.

The emergence of dry point contact (DPC) transducers has made ultrasonic NDT of concrete members more efficient by eliminating the need for coupling agents for the transmission of energy to the test specimens. Data acquisition systems integrating multiple DPC sending and receiving transducers have further increased the efficiency of collecting data [4]. These systems provide a large amount of data in a fraction of a second. Development of DPC transducers emitting horizontal shear waves offered a significant advancement in NDT of concrete structures. While most of the energy of longitudinal signals converts to shear and surface waves after transmission [4], horizontal shear waves preserve a higher level of energy while propagating in concrete, and therefore, permit greater penetration depth. The lower wavelength of shear waves in comparison to longitudinal waves and higher energy level of shear waves permit detection of smaller inclusions and defects at deeper depths in low frequencies. This technology is extensively used in practice to measure thickness and to detect rebar, delamination, and damage [5–12].

The main challenge in ultrasonic NDT of concrete structures is the composite nature of concrete. The heterogeneity of concrete can cause scattering of propagating ultrasonic waves [13]. Scattering attenuates the energy of the coherent waveforms (scattering attenuation) and limits the penetration depth of the ultrasonic waves. Scattering attenuation is correlated with the ratio of the aggregate size to the wavelength of the transmitted wave [13]. The velocity of shear wave in concrete is about 2500 m/s, while the velocity of longitudinal wave is around 4300 m/s [2]. The lower wavelength of shear wave in the hosting medium ($\lambda = c/f$, where λ is wavelength, $c$is velocity and f is frequency) increases the potential of scattering of shear waves in concrete. Due to the broad applications of data acquisition systems that employ DPC shear transducers in practice, and since the signal to noise ratio (SNR) plays a significant role in the detection of inclusions and defects, as well as geometry measurements, gaining insight into the scattering attenuation of horizontal shear waves is vital. Several numerical and experimental investigations have been conducted to understand the scattering attenuation of longitudinal waves in concrete [14–18]; however, to our knowledge, the literature lacks a study on the scattering attenuation of shear waves.

In this study, we used numerical simulations to study the effect of shape, size and material properties of aggregates on the scattering attenuation of shear waves in concrete. We used a simple approach to

---

[*] Corresponding author.
E-mail address: aziz@umn.edu (A. Asadollahi).

https://doi.org/10.1016/j.ultras.2018.07.011
Received 19 April 2018; Received in revised form 12 July 2018; Accepted 19 July 2018

generate non-overlapping aggregates and voids and considered them in numerical simulations to investigate the influence of heterogeneity on attenuation of shear waves in concrete. Because the frequency range of 20–150 kHz is generally used in practice [2], we studied the scattering attenuation in this frequency range. To investigate the effect of shape and material properties of aggregates, we assumed that the aggregates could be ellipsoidal, representing rounded aggregates, or rectangular cuboid, representing angular aggregates, in shape and can have two different material properties. Furthermore, we considered synthetic concrete specimens with and without air voids to investigate the effect of porosity on the scattering attenuation. Because the range of application of ultrasonic testing is broad, it can be applied to concrete pavements, bridges, tunnel linings, foundations, etc., and since the maximum aggregate size in these structures can be different, we chose the maximum aggregate sizes of 18, 25, and 38 mm in the mix design of the synthetic concrete specimens to investigate the effect of aggregate size on scattering attenuation. We performed the same simulations for longitudinal waves and compared the scattering attenuation of shear and longitudinal waves in the synthetic concrete specimens. To perform the numerical simulations, we developed a 3D numerical tool. We used the finite integration technique (EFIT) [19] for the spatial discretization of the governing equations. We employed perfectly matched layers to truncate the computational medium. It is worth mentioning that the accuracy of the EFIT in simulating the propagation of waves in a concrete medium was shown in [14,15]; we do not validate EFIT in this paper.

The rest of the paper is arranged as follows. First, we discuss the methods introducing the EFIT, giving the formulation of the perfectly matched layer, and presenting the approach used to generate the non-overlapping aggregates. Next, we present the simulation results and discussion.

2. Methods

2.1. Elastodynamic finite integration technique

We developed a numerical tool to simulate wave propagation in concrete. FORTRAN was used for programming, and Elastodynamic Finite Integration Technique (EFIT) for spatial discretization of the differential equations. To use EFIT for discretization, Cauchy's equation of motion (Eq. (1)) and Hook's law (Eq. (2)) are written in terms of velocity and stress:

$$\rho \dot{v}_i = \sigma_{ij,j}, \tag{1}$$

$$\dot{\sigma}_{ij} = \lambda \delta_{ij} v_{k,k} + \mu v_{i,j} \tag{2}$$

where ρ is mass density, σ_{ij} are stress tensor components, v_i are velocity components, and λ and μ are Lamé constants. EFIT integrates the governing equations over each integration cell:

$$\int_{V_c} \rho \dot{v}_i dV = \int_{\partial V_c} \sigma_{ij} n_j dS, \tag{3}$$

$$\int_{V_c} \dot{\sigma}_{ij} dV = \int_{\partial V_c} (\lambda \delta_{ij} v_k n_k + \mu v_i n_j) dS. \tag{4}$$

The discretization is performed by estimating Eqs. (3) and (4) over the cell volume and boundaries using a one-point Gaussian quadrature rule. Here, we assume that the cells are cubic in shape and they have the same size. The arrangement of stress and velocity components in 3D is shown in Fig. 1 [15]. Note that in this study $\Delta x = \Delta y = \Delta z$. Velocity and stress components are located at different spatial places (Fig. 1). These components are located in the center of the corresponding integration cells. Material parameters of the heterogeneous concrete are defined on a spatial grid that matches the grid representing the center of σ_{ii}cells. A special averaging is used to estimate the material parameters at the location of velocities and shear stresses [20,21]. A Leapfrog scheme is used for time integration (Eqs. (5) and (6)):

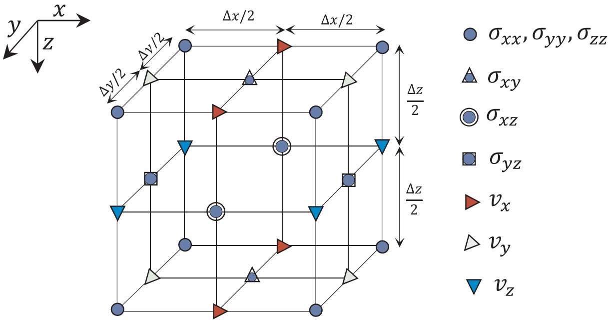

Fig. 1. Arrangement of stress and velocity components in EFIT.

$$v_i^{m+1/2} = v_i^{m-1/2} + \dot{v}_i^m \Delta t, \tag{5}$$

$$\sigma_{ij}^{m+1} = \sigma_{ij}^m + \dot{\sigma}_{ij}^{m+1/2} \Delta t. \tag{6}$$

To minimize the numerical dispersion, the following expression should be satisfied [21]:

$$max\ \ (\Delta x,\, \Delta y,\, \Delta z) \le \frac{1}{8}\lambda_{min} = \frac{1}{8}\frac{c_{min}}{f_{max}} \approx \frac{1}{10}\frac{c_{s,min}}{f_{max}}, \tag{7}$$

where c_{min} is the minimum wave speed in the medium, $c_{s,min}$ is the minimum shear wave speed in the medium, and f_{max} is the maximum frequency in the spectrum of the emitted signal. To avoid numerical instability, Eq. (8) has to be fulfilled [19].

$$\Delta t \le \frac{1}{c_{max}\sqrt{\frac{1}{\Delta x^2} + \frac{1}{\Delta y^2} + \frac{1}{\Delta z^2}}}, \tag{8}$$

c_{max} in Eq. (8) is the maximum wave speed in the medium. Assuming that $\Delta x = \Delta y = \Delta z$, Eq. (8) can be simplified to Eq. (9).

$$\Delta t \le \frac{\Delta x}{\sqrt{3}\, c_{max}}. \tag{9}$$

It is worth mentioning that EFIT is virtually the same as a second-order velocity-stress finite difference on a staggered grid. Higher order finite difference methods allow using a coarser spatial grid, but a fine spatial grid is required for representing the strong heterogeneity of concrete. Therefore, EFIT is the most efficient technique for the simulation of wave propagation in this material.

2.2. Implementation of perfectly matched layers

Perfectly matched layers (PML) [22–24] were implemented in the program and assigned to the boundaries with faces perpendicular to the x and y-directions to truncate the computational domain laterally (Fig. 2).

The amplitude of the outgoing waves decays exponentially in the PML by employing a damping profile. The value of damping at the interface of the medium and absorbing layer is zero in the perfectly matched layer, material properties of PML and computational medium match perfectly in the interface, and as moving into the absorbing layer the damping is gradually increased. A fixed boundary condition can be assigned to the outer boundary of a perfectly matched layer. The layers have to be thick enough to dampen virtually all of the energy of the outgoing waves. Here, we implemented the formulation for PML given in [24]. To facilitate use of formulation, we present the equation of motion (Eq. (10)) and constitutive equation (Eq. (12)) in the perfectly matched layers for an isotropic media. θ and ζ in Eqs. (10) and (12) are called memory variables which are evaluated from Eqs. (11) and (13). The equations after time integration using leap-frog scheme are shown:

$$\rho v_i^{m+1/2} = \rho v_i^{m-1/2} + \Delta t\left(c_p \delta_{jp} \sigma_{ij,j}^m + (1-\delta_{jp}) \sigma_{ij,j}^m + d_p \theta_i^{m-\frac{1}{2},p}\right), \tag{10}$$

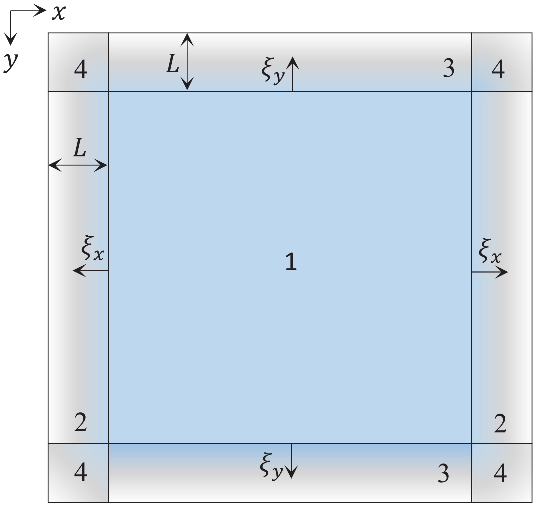

Fig. 2. Perfectly matched layers used to truncate computational domain laterally.

$$\theta_i^{m+1/2,p} = f_p\theta_i^{m-1/2,p} - e_p\delta_{jp}\sigma_{ij,j}^m, \tag{11}$$

$$\sigma_{ij}^{m+1} = \sigma_{ij}^m + \Delta t\left(c_p\lambda\delta_{ij}\delta_{kp}v_{k,k}^{m+\frac{1}{2}} + c_p\mu\delta_{jp}v_{i,j}^{m+\frac{1}{2}} + c_p\mu\delta_{ip}v_{j,i}^{m+\frac{1}{2}} + \lambda(1-\delta_{kp})\delta_{ij}v_{k,k}^{m+\frac{1}{2}} + \mu(1-\delta_{jp})v_{i,j}^{m+\frac{1}{2}} + \mu(1-\delta_{ip})v_{j,i}^{m+\frac{1}{2}} + d_p\zeta_{ij}^{m,p}\right), \tag{12}$$

$$\zeta_{ij}^{m+1,p} = f_p\zeta_{ij}^{m,p} - e_p\left(\lambda\delta_{ij}\delta_{kp}v_{k,k}^{m+\frac{1}{2}} + \mu\delta_{jp}v_{i,j}^{m+\frac{1}{2}} + \mu\delta_{ip}v_{j,i}^{m+\frac{1}{2}}\right). \tag{13}$$

Assuming that the value of γ in [24] is one, c_p, d_p, e_p, and f_p are given in the following equations:

$$c_p = 1 - \frac{\Omega_p\Delta t}{g_p};\ d_p = \frac{2}{g_p};\ e_p = \frac{4-g_p}{g_p};\ f_p = -2(1-c_p), \tag{14}$$

where g_p: $=2 + (\alpha + \Omega_p)\Delta t$. The value of α is chosen to be πf_c where f_c is the center frequency of the emitted signal. We also assumed that $\Omega_p = \Omega_o(\xi_p/L)^2$, where ξ_p is originated from the interface of computational medium and PML and is oriented perpendicular to the interface, p indicates the direction of ξ_p; L is the thickness of the absorbing layer. Note that p is x in region two of Fig. 2, it is y in region three, and is x and y in region four. Region one represents the truncated medium. For clarity, we provided the equation for σ_{xx} and its memory variables in region two and four of Fig. 2. In region two, σ_{xx} is:

$$\sigma_{xx}^{m+1} = \sigma_{xx}^m + \Delta t\left(c_x(\lambda + 2\mu)v_{x,x}^{m+\frac{1}{2}} + \lambda v_{y,y}^{m+\frac{1}{2}} + \lambda v_{z,z}^{m+\frac{1}{2}} + d_x\zeta_{xx}^{m,x}\right), \tag{15}$$

$$\zeta_{xx}^{m+1,x} = f_x\zeta_{xx}^{m,x} - e_x(\lambda + 2\mu)v_{x,x}^{m+\frac{1}{2}}, \tag{16}$$

and in region four, σ_{xx} is:

$$\sigma_{xx}^{m+1} = \sigma_{xx}^m + \Delta t\left(c_x(\lambda + 2\mu)v_{x,x}^{m+\frac{1}{2}} + c_y\lambda v_{y,y}^{m+\frac{1}{2}} + \lambda v_{z,z}^{m+\frac{1}{2}} + d_x\zeta_{xx}^{m,x} + d_y\zeta_{xx}^{m,y}\right), \tag{17}$$

$$\zeta_{xx}^{m+1,x} = f_x\zeta_{xx}^{x,m} - e_x(\lambda + 2\mu)v_{x,x}^{m+1/2}, \tag{18}$$

$$\zeta_{xx}^{m+1,y} = f_y\zeta_{xx}^{y,m} - e_y(\lambda + 2\mu)v_{x,y}^{m+1/2} \tag{19}$$

2.3. Generation of non-overlapping aggregates and air voids

Aggregates and voids have to be modeled explicitly in the numerical simulations in order to take scattering attenuation into account. Recently, several algorithms have been proposed for generating non-overlapping aggregates and voids and using them in the finite element models [25–28]. In this paper, we present a simple approach in that we use the material grid of EFIT to generate aggregates and voids. In this approach, we generate the 3D material grid that covers the computational domain and we assign a single number to all grid points, which represents the background material, cement matrix in our case. Each time an aggregate or void with a random size and a random location is generated, the material numbers assigned to the grid points surrounded by the new aggregate or void's boundary are examined. If all numbers are equal to the material number of the cement matrix, then the location is determined to be available. In this case, we assign the material number associated with the new aggregate's or void's material properties to the grid points located in the aggregate. Otherwise, the location is preoccupied by another aggregate or void. In this case, a new location must be assigned to the aggregate or void and the availability of the new location for placing the aggregate or void must be checked. This process continues until a certain volume of the concrete specimen is occupied by aggregates and voids. Note that each material number defines a different material, and each aggregate can be defined with a different material number.

2.3.1. Some hints for generating non-overlapping aggregates and voids

The following hints can be helpful when generating aggregates and voids.

- Aggregates and voids should be generated from coarse to fine. If finer aggregates or voids were to be generated first, it would be impossible to find free locations for coarser aggregates or voids.
- It is not necessary to check material numbers of all grid points inside the aggregate to examine whether the place was previously occupied. When looping over grid points in the x-direction, for example, the increment step of the loop can be the number of grid points in 1/10 of aggregate size in the x-direction. By doing so, the computation burden can be decreased significantly.
- If the size of the spatial grid being used is very small, a multigrid approach can be used to generate the aggregates and voids. A coarse grid can be used to generate the coarse aggregates. Then, save the geometry and location of those in memory. Next, assign the material number of the saved aggregates to the fine grid. Finally, generate the fine aggregates using the fine grid.
- To generate aggregates at a specific distance from a boundary or to avoid generating aggregates and voids in a specific region, assign a number, which is different from the material number of cement matrix, to the region where the presence of aggregates and voids should be avoided. Then, generate aggregates and voids. Subsequently, the material number in the avoided region can be changed back to the material number of the material occupying that region.

In the following sections, we explain how to generate ellipsoidal and cuboid aggregates.

2.3.2. Generation of an ellipsoidal and a cuboid aggregate

Suppose that we want to generate an ellipsoidal aggregate with semi-axes of length a, b, and c, with a center at (x_c, y_c, z_c), and with principal axes that form the angles of α, β, and γ with the x, y, and x-axes, respectively. To this end, first we generated a standard ellipsoid by randomly generating the numbers a, b,and c. Here, we assume that $0.5a \le b$, $c \le a$. Then, we generated three random numbers, (x_c, y_c, z_c), that represent the center of the ellipsoid, and we transfer the center of the standard ellipsoid to this point. Afterward, the principal axes of the standard ellipsoid are rotated about x, y, and z-axes by angles α, β and γ, respectively. The rotation matrix is given by Eq. (20):

$$R = R_z R_y R_x = \begin{bmatrix} cos\beta cos\gamma & -cos\alpha sin\gamma + sin\alpha sin\beta cos\gamma & sin\alpha sin\gamma + cos\alpha sin\beta cos\gamma \\ cos\beta sin\gamma & cos\alpha cos\gamma + sin\alpha sin\beta sin\gamma & -sin\alpha cos\gamma + cos\alpha sin\beta sin\gamma \\ -sin\beta & sin\alpha cos\beta & cos\alpha cos\beta \end{bmatrix}, \tag{20}$$

where R_x, R_y and R_z are rotation matrices about the x, y and z axis, respectively. Coordinates in the transferred and rotated system are obtained from $\boldsymbol{x}' = R\boldsymbol{x}$ where $\boldsymbol{x}^T = (x{-}x_c, y{-}y_c, z{-}z_c)$. Point $(\boldsymbol{x}')^T = (x', y', z')$ is in the transferred and rotated ellipsoid if:

$$(x'/a)^2 + (y'/b)^2 + (z'/c)^2 \le 1. \tag{21}$$

To produce a cuboid aggregate, we first generated three random numbers (a, b, and c) representing the lengths of the edges of the cuboid. Here, we assumed that $0.5a \le b, c \le a$. Then, we randomly generated the coordinates of a vortex of the cuboid. Next, we generated three unit vectors that start from a vortex of the cuboid to define the direction of the edges. These three unit vectors can be multiplied with a, b, and c, and used to obtain the coordinates of other vortices of the cuboid. The first unit vector was generated by producing three random numbers in the range of $[-1, 1]$. This vector was then normalized to obtain the first unit vector. To generate the second unit vector, two random numbers were generated in the range of $[-1, 1]$. Then, the third component of the vector was obtained from the orthogonality of the two edges of the cube. The second vector was normalized to obtain the second unit vector. The third unit vector is simply obtained from the cross product of the first and second unit vectors.

2.3.3. Examining the material number of grid points inside cuboid and ellipsoidal aggregates

We want to check the material numbers of grid points located inside a cuboid aggregate. To do this, we determine the minimum and maximum of the aggregate vortices' coordinate data. We denote this coordinates with x_{min}, x_{max}, y_{min}, y_{max}, z_{min}, and z_{max}. New vortices at $(x_{min}, y_{min}, z_{min})$ and $(x_{max}, y_{max}, z_{max})$ define a cuboid that surrounds the cuboid aggregate. We loop over all grid points located inside the surrounding cuboid to determine the points that are located inside the cuboid aggregate. To examine if a point is inside a newly generated aggregate, we obtain the dot product of the three unit vectors representing the direction of the edges of the aggregate ($\boldsymbol{e}_a$, $\boldsymbol{e}_b$, and $\boldsymbol{e}_c$) with a vector that starts from the vortex where the unit vectors start and ends at the point of interest ($\boldsymbol{v}$) (Fig. 3).

If the following conditions hold (Eq. (22)), then the point is in the aggregate.

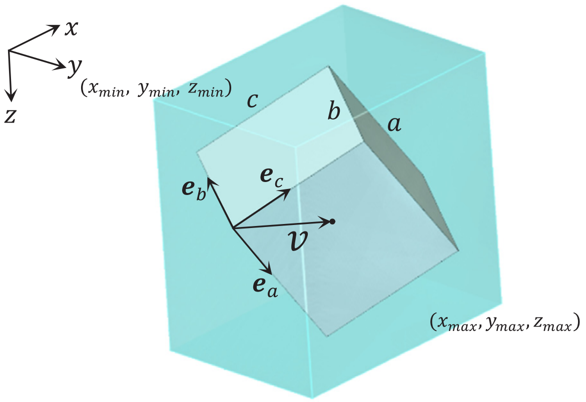

Fig. 3. A cuboid aggregate is surrounded by the vertical cuboid.

$$0 \le \boldsymbol{e}_a \cdot \boldsymbol{v} \le a \;\; and \;\; 0 \le \boldsymbol{e}_b \cdot \boldsymbol{v} \le b \;\; and \;\; 0 \le \boldsymbol{e}_c \cdot \boldsymbol{v} \le c. \tag{22}$$

Otherwise, it is located outside of the aggregate. If the point is inside the aggregate, we check the material number assigned to that point for overlapping control.

For an ellipsoidal aggregate, we generate a cuboid that surrounds it. Then we loop over all points inside the cuboid. A point is inside the ellipsoidal aggregate if it satisfies Eq. (21). If the point is inside the ellipsoid, we check the material number assigned to that point.

Images of two specimens with ellipsoidal and cuboid aggregates generated using the explained approach are depicted in Fig. 4.

3. Results and discussion

Some authors assume concrete is a homogeneous material when the frequency of emitted signals is in the range of 20–150 kHz [29]. However, the experimental data shows the scattering attenuation of shear waves in concrete within this frequency range. Fig. 5 represents the data collected by a linear array device, MIRA (see [5] for the details of the device), from a concrete slab with the thickness of 210 mm. The center frequency of the transmitted signal was 50 kHz and the receiving channel of transducers was located at the distance of 120 mm from the transmitting channel of transducers, both located on the same side of the slab. As can be seen from Fig. 5, the amplitude of the noise is large and is decreasing at the time window of 170 µs to 820 µs. The main reason for the large amplitude noise in this time interval is scattering of incident waves by aggregates, and the reason for the decrease in its amplitude is geometric-spreading. The level of the noise is virtually constant for t > 820 µs; this noise is primarily environmental. As can be observed, even for a signal with the center frequency of 50 kHz the level of structural noise, the noise caused by scattering, is considerable.

Note that 2D simulations result in a low signal-to-noise ratio and cannot be used to study the effect of heterogeneity of concrete on the scattering attenuation. In 2D simulations, waves are enforced to scatter in the same plane they were transmitted. Therefore, the acquired data become unrealistically noisy. In a real concrete specimen, the random shapes and orientations of aggregates cause scattering of the incident waves in all directions in the 3D space. Moreover, the previous studies on longitudinal waves show higher scattering attenuation in 2D simulations [15]. Thus, 3D numerical simulations were performed to investigate scattering attenuation in this study.

3.1. Influence of shape, size and material properties of aggregates on scattering attenuation

We restricted the attenuation to scattering attenuation by transmitting the source signal from all points located on the top surface of the synthetic specimens. The size of the synthetic specimens in x and y directions were set large enough to guarantee that the condition of 1D wave propagation would hold for the points located in a neighborhood of the computational domain center during the recording time. In all numerical simulations, the size of the specimens in the x and y-directions were 0.9 m and the depth of the specimens was 0.30 m. We assumed that the top and bottom boundaries of the numerical specimens were free and perfectly matched layers were assigned to the lateral boundaries. The thickness of the perfectly matched layer was 20 grid spacing in this study.

We assumed that the maximum sizes of ellipsoidal and cuboid aggregates were 19, 25 and 38 mm. We used Fuller's 0.45 power curve [25] to fill 50% of the volume of the concrete with aggregates. Using the approach introduced in Section 2.3, we could generate more than 200,000 of non-overlapping aggregates and voids in less than a minute. We defined two types of materials for aggregates, where the difference of the acoustical properties of the first type of aggregates with the cement matrix was lower than that of the second type [15]. In this paper, we refer to the aggregates made of the first material as "aggregate type

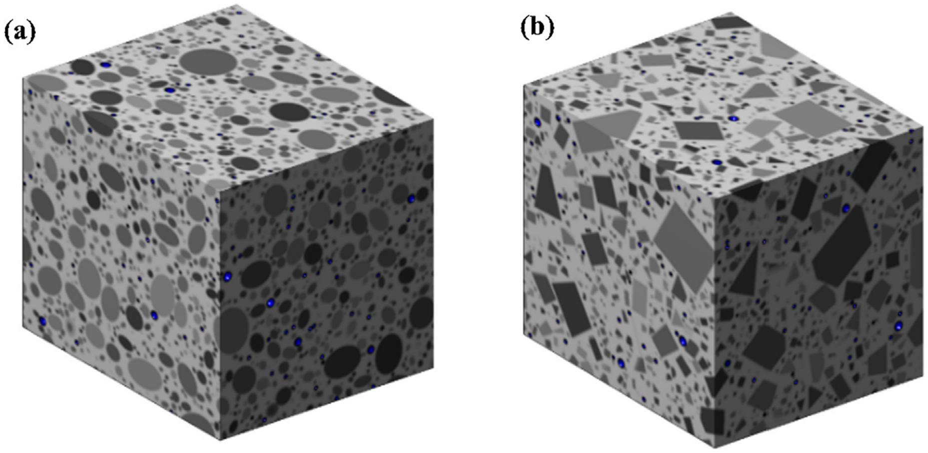

Fig. 4. 3D numerical concrete specimens with (a) ellipsoidal and (b) cuboid aggregates.

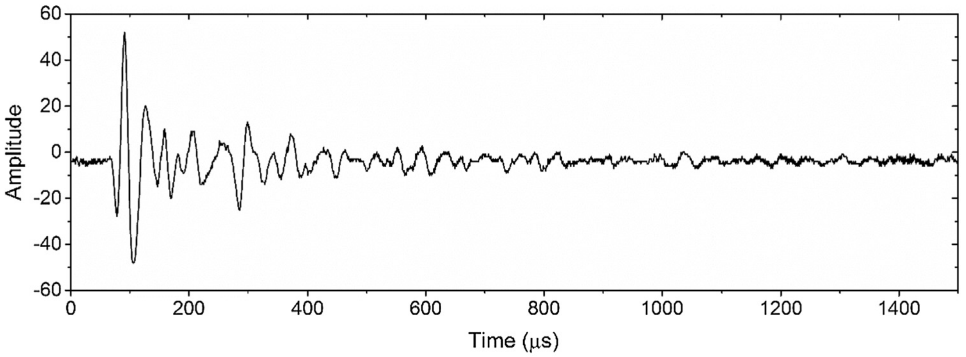

Fig. 5. Signal recorded by a receiving channel of transducers at the distance of 120 mm from a sending channel of transducers.

Table 1
Material properties of cement matrix and aggregates.

Material Properties	Cement Matrix	Aggregate Type One	Aggregate Type Two	Air
Density (kg/m^3)	2050	2610 $+130\eta_1$	2950	1.20
Shear Velocity (m/s)	2250	2450 $+ 125\eta_2$	3330	0
Longitudinal Velocity (m/s)	3950	4180 $+210\eta_3$	5730	0

one” and the aggregates made of the second material as “aggregate type two”. The material properties of cement matrix and the two types of aggregates are given in Table 1. η_1, η_2, and η_3 in Table 1 are random numbers uniformly distributed in the range of [-1, 1]. It was assumed that 1% of the volume of the synthetic concrete specimens was filled with spherical air voids with the diameter of 2 mm [30]. We assigned the material properties provided in Table 1 to air voids and treated them similarly to aggregates in the numerical simulations.

The transmitted wavelet was assumed to be the RC2 signal given by Eq. (23):

$$RC2(t) = (1-\cos(\pi f_c t))\cos(2\pi f_c t), \quad 0 \le t \le 2/f_c, \tag{23}$$

where f_c is the center frequency of the signal. Since EFIT uses velocities and stresses as prescribed values, the normalized first time derivative of the RC2 signal (Fig. 6) was used as prescribed velocity.

The transmission of horizontal shear waves to the computational domain was performed by assigning the normalized wavelet, as the y-component of velocity, to the center of all v_y cells (Fig. 1) located on the top surface ($z = 0$) of the synthetic specimens. Twenty-five points located at a depth of 0.15 m and distributed on a structured grid with the grid spacing of 0.02 m were used to record the y-component of velocity as output signals. The center of the specimen matched the center of the grid. The sampling rate was 10 MHz. The average of the recorded signals was used to evaluate scattering attenuation. Using averaging the structural noise is filtered from the recorded signals. The attenuation was obtained by using Eq. (24) [18]:

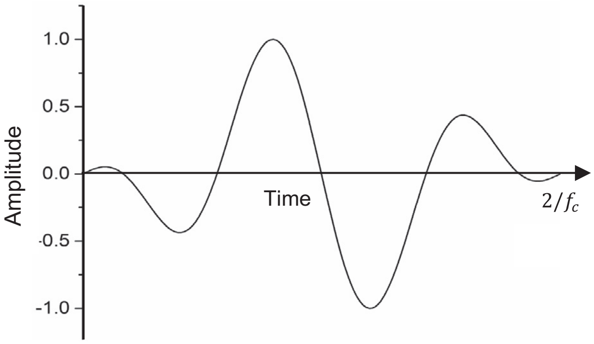

Fig. 6. The transmitted wavelet.

$$\alpha = -\frac{20}{x}\log_{10}\frac{A_x(f_c)}{A_0(f_c)}, \tag{24}$$

where $A_x(f_c)$ is the amplitude associated with the frequency f_c (Eq. (23)) in the frequency spectrum of the first arrival signal recorded at distance x from emitter. Frequency spectrum is obtained by applying fast Fourier transform (FFT) to the recorded signal. $A_o(f_c)$ is the peak amplitude of the emitted signal, which is associated to the frequency f_c in the frequency spectrum of the RC2 signal (Eq. (23)). We obtained the attenuation corresponding to the transmitted signals with the center frequency of 25, 50, 75, 100, 125, and 150 kHz using Eq. (24); then we

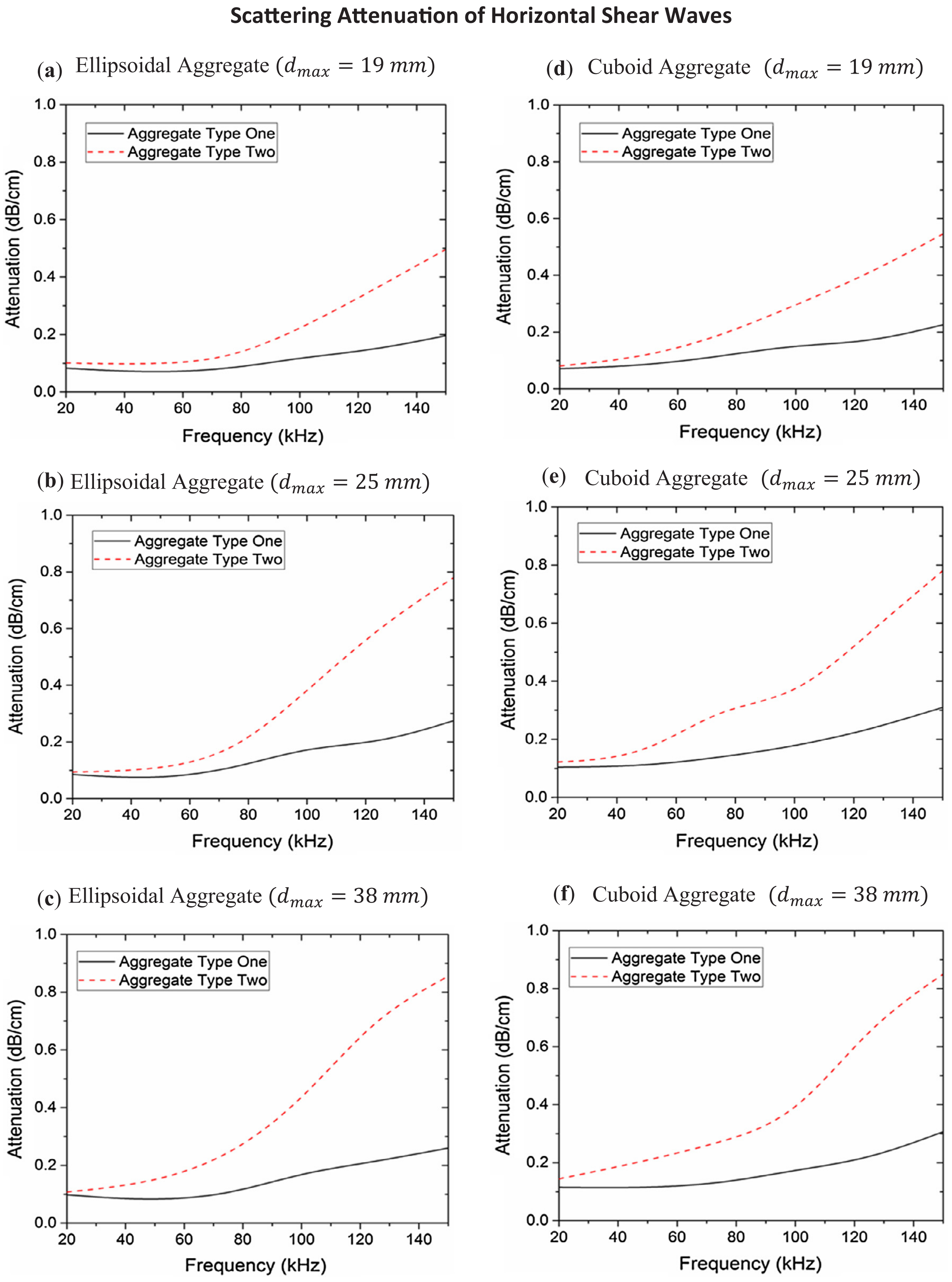

Scattering Attenuation of Horizontal Shear Waves

(a) Ellipsoidal Aggregate ($d_{max} = 19\ mm$)

(b) Ellipsoidal Aggregate ($d_{max} = 25\ mm$)

(c) Ellipsoidal Aggregate ($d_{max} = 38\ mm$)

(d) Cuboid Aggregate ($d_{max} = 19\ mm$)

(e) Cuboid Aggregate ($d_{max} = 25\ mm$)

(f) Cuboid Aggregate ($d_{max} = 38\ mm$)

Fig. 7. Scattering attenuation of shear waves versus center frequency of emitted signals for synthetic concrete specimens with ellipsoidal aggregates with maximum size of (a) 19mm, (b) 25mm and (c) 38mm, and for synthetic concrete specimens with cuboid aggregates with maximum size of (d) 19mm, (e) 25mm, and (f) 38mm.

fitted a curve to these six values to provide the attenuation curves.

Maximum frequency in the frequency spectrum of RC2 signal with the center frequency of f_c is virtually $2f_c$, therefore, for $f_c = 150$kHz and material parameters provided in Table 1 conditions in Eqs. (7) and (9) lead to $\Delta x \leq 0.0075m$ and $\Delta t \leq 0.075\mu s$. We chose $\Delta x = 0.005m$ and $\Delta t = 0.05\mu s$ in all numerical simulations in this study.

The numerical simulations were performed and the scattering attenuation was computed for the given frequency range (Fig. 7). Maximum aggregate size was denoted by d_{max} in Fig. 7. As can be observed from the graphs presented in Fig. 7, the scattering attenuation was strongly dependent on the maximum aggregate size. Evidently, the scattering attenuation was larger for aggregates with a maximum size of 38 mm. For aggregates with maximum sizes of 25 mm and 38 mm, as the frequency increased, the difference in the value of scattering

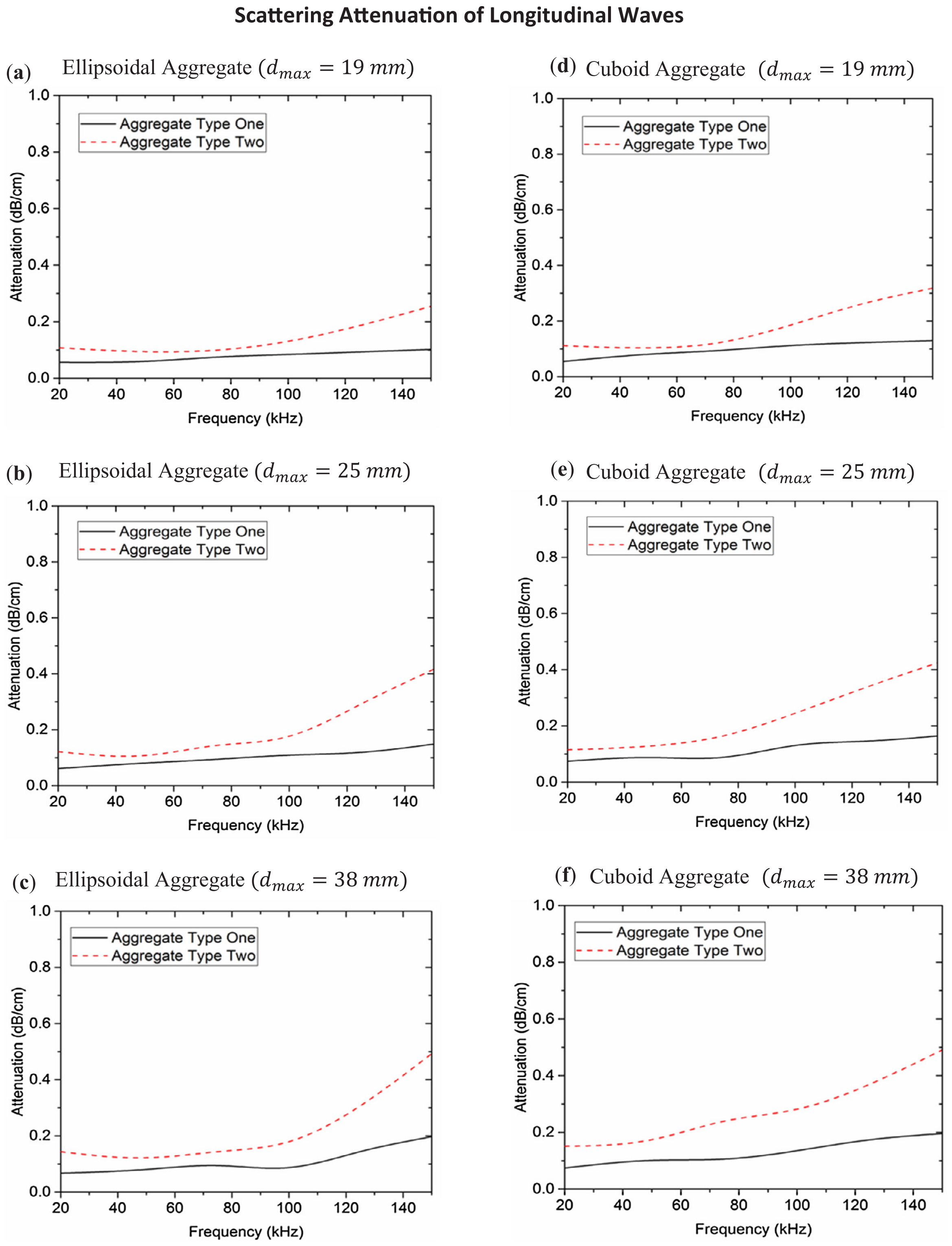

Fig. 8. Scattering attenuation of longitudinal waves versus center frequency of emitted signals for synthetic concrete specimens with ellipsoidal aggregates with maximum size of (a) 19mm, (b) 25mm and (c) 38mm, and for synthetic specimens with cuboid aggregates with maximum size of (d) 19mm, (e) 25mm and (f) 38mm.

attenuation decreased.

Fig. 7 illustrates that the type two aggregates caused significantly larger scattering attenuation in comparison with type one aggregates, and as the center frequency of the emitted signal increased, the effect of the material properties of aggregates on the scattering attenuation increased. For all types and sizes of aggregates, the scattering attenuation was small for emitted signals with center frequencies lower than 50 kHz; for type one aggregates, this range was larger. Velocity of shear wave in the synthetic concrete specimens was computed to investigate the influence of aggregates' shape, size, and material properties on the velocity of the shear wave in concrete. To do so, we transmitted shear waves from a point on the top surface of the specimen and recorded the first arrival signals by the receivers located on the top surface of the specimens in a plane that contained the sender and was perpendicular

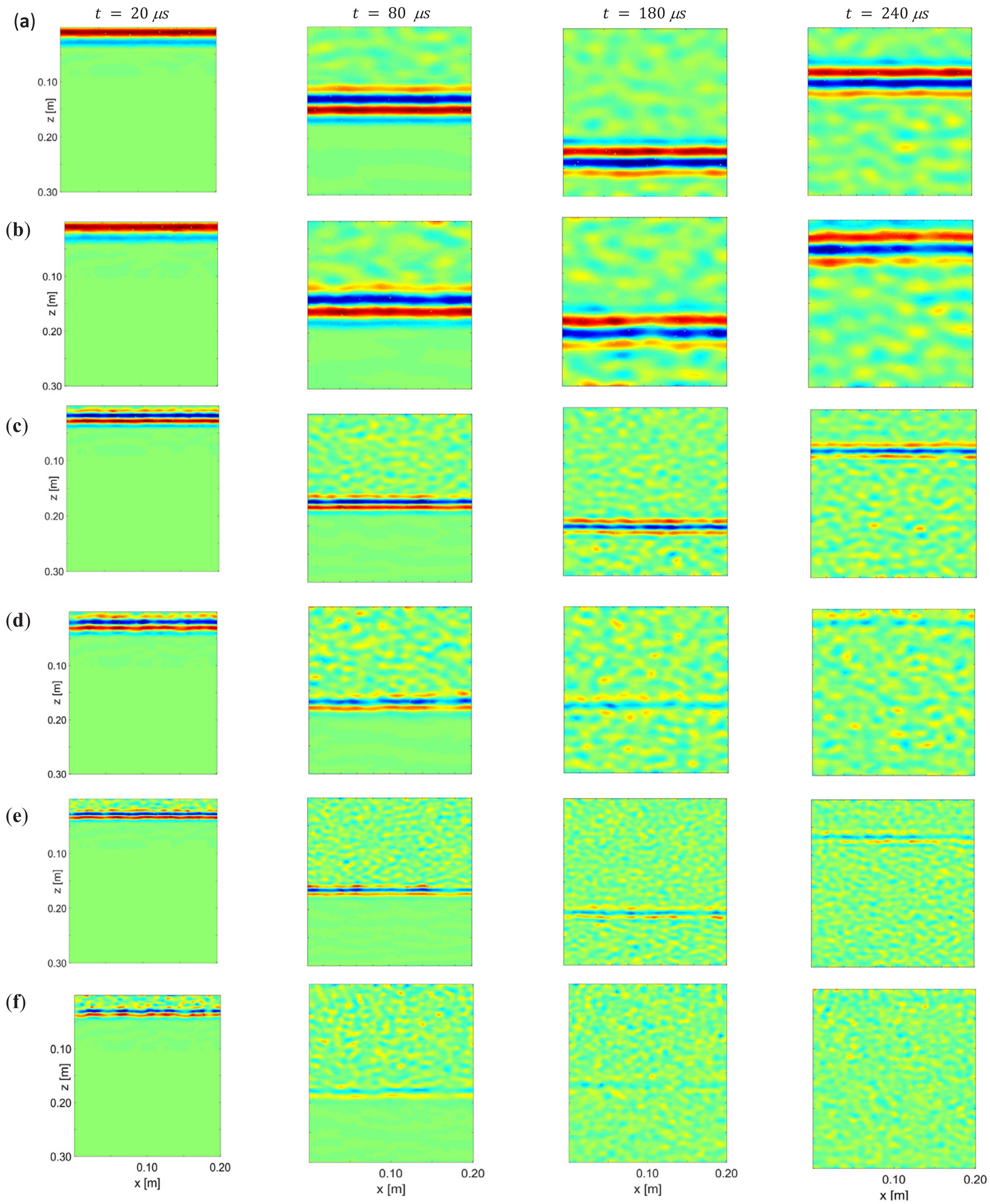

Fig. 9. Snapshots taken at t = 20, 80, 180, and 240 μs from the propagation of horizontal shear waves in synthetic concrete specimens with ellipsoidal aggregates (d_{max} = 25mm) of (a) type one (f_c = 50kHz), (b) type two (f_c = 50kHz), (c) type one (f_c = 100kHz), (d) type two (f_c = 100 kHz), (e) type one (f_c = 150kHz), and (f) type two (f_c=150kHz).

to the y-axis. Having the distances of receivers and the travel time of the emitted signal from the first to the second receiver, the velocity of the shear wave was computed. The results showed that the velocity of the shear wave was virtually not dependent on the size or shape of aggregates. The velocity of the shear wave in the concrete specimens with aggregate type one was about 2350 m/s. This value for concrete made of aggregate type two was around 2550 m/s. Apparently, the velocities of the shear waves in two specimens were not considerably different. However, the scattering attenuation was significantly larger in the concrete specimen made of aggregate type two.

The simulation results (Fig. 7) show that the scattering attenuation was slightly affected by the shape of the aggregates. The scattering attenuation in the synthetic concrete specimens with cuboid aggregates was slightly larger than that in synthetic specimens with the ellipsoidal aggregates.

We performed the same numerical experiments for longitudinal waves (Fig. 8) by exciting the top surface of the synthetic concrete specimens in the z-direction. The same behavior as horizontal shear

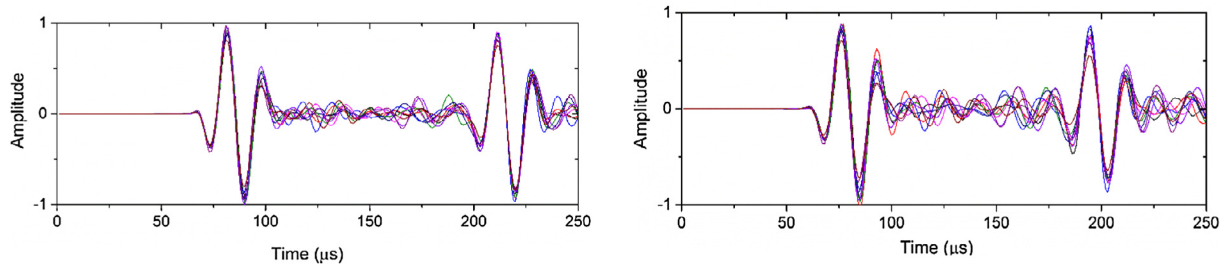

(a) Aggregate type one ($f_c = 50\ kHz$)

(b) Aggregate type two ($f_c = 50\ kHz$)

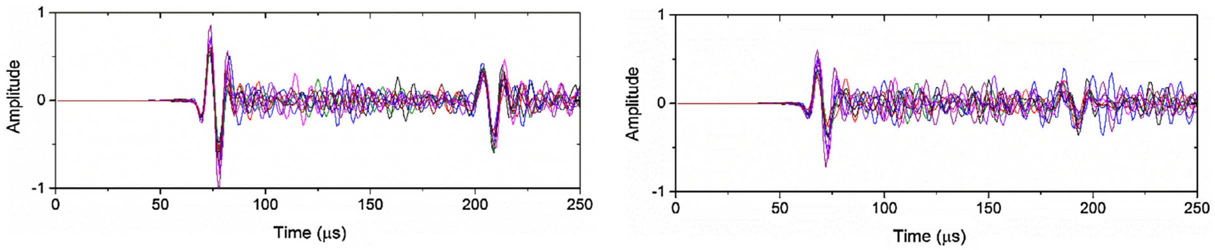

(c) Aggregate type one ($f_c = 100\ kHz$)

(d) Aggregate type two ($f_c = 100\ kHz$)

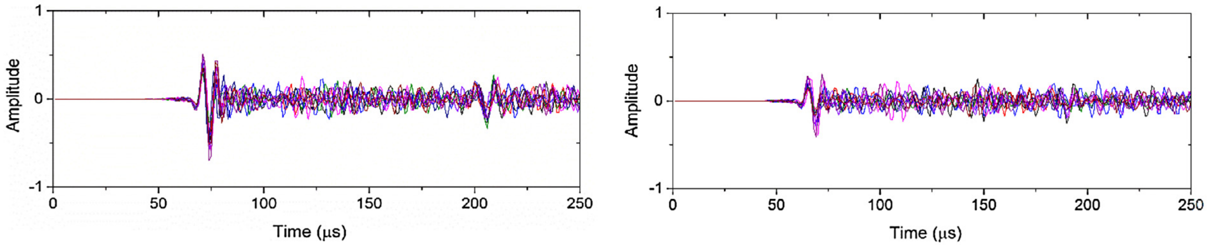

(e) Aggregate type one ($f_c = 150\ kHz$)

(f) Aggregate type two ($f_c = 150\ kHz$)

Fig. 10. Waveforms recorded at nine different points at $z = 0.15$m synthetic of specimens with ellipsoidal aggregates ($d_{max} = 25$mm) of (a) type one ($f_c = 50$kHz), (b) type two ($f_c = 50$kHz), (c) type one ($f_c = 100$kHz), (d) type two ($f_c = 100$kHz), (e) type one (f_c=150kHz), and (f) type two ($f_c = 150$ kHz).

waves can be observed for longitudinal waves. However, the scattering attenuation was smaller for longitudinal waves.

For synthetic concrete specimens with type one aggregates (Fig. 8), the scattering attenuation of longitudinal waves was insignificant for the three aggregate sizes for frequencies lower than around 80 kHz. For higher frequencies, the attenuation was virtually one-half of that for horizontal shear waves for synthetic concrete specimens with both cuboid and ellipsoidal aggregates. For synthetic concrete specimens with type two aggregates, the scattering attenuation was significantly larger than that for the specimens with type one aggregates. For these specimens and for aggregate with the size of 38 mm the attenuation of longitudinal waves was large for frequencies higher than 100 kHz. However, comparing the graphs in Figs. 7 and 8, the attenuation of longitudinal waves was still noticeably lower than that for horizontal shear waves.

The y-component of velocity wavefields (horizontal shear waves) at four different times are presented in Fig. 9. Numerical simulations were performed on specimens with ellipsoidal aggregates with the maximum size of 25 mm to provide the snapshots. The snapshots show transmitted wavelets with the center frequencies of 50 kHz, 100 kHz, and 150 kHz. The waveforms recorded by nine receivers located at the depth of 150 mm are provided in Fig. 10. As can be observed from Figs. 9 and 10, the scattering attenuation of horizontal shear waves at the center frequency of 50 kHz was low and the transmitted wave kept most of its energy when it reached the top boundary. At higher frequencies, the scattering attenuation was considerable. At the center frequency of 150 kHz, for example, the coherent wave lost virtually all its energy after traveling 0.6 m in a concrete specimen made of type two aggregates. It can be seen from Fig. 9 that the scattering attenuation was path dependent. In the case where the incident waves met larger aggregates in their way, the scattering attenuation was larger.

3.2. Influence of air voids on scattering attenuation

In all simulations presented previously, one percent of the synthetic concrete specimens' volume was filled by air voids. To investigate the effect of air voids on scattering attenuation, we removed the air voids and performed the simulations on the synthetic specimens with ellipsoidal aggregates and obtained the scattering attenuation (Fig. 11). By comparing the graphs in Fig. 11a, b and c with those in Fig. 7a, b and c, one can deduce that air voids had more influence on scattering attenuation of horizontal shear waves at higher frequencies; their influence in frequencies lower than 80 kHz was negligible. The influence of air voids on scattering attenuation of horizontal shear waves was more noticeable for synthetic concrete specimens made of type one aggregates. Air voids had a negligible effect on the scattering attenuation of longitudinal waves (Fig. 11d–f).

4. Conclusions

This study has shown that the scattering attenuation of horizontal shear waves is correlated to size and material properties of the aggregates in the frequency range of 20 kHz to 150 kHz. We found that the scattering attenuation was slightly larger for cuboid aggregates, representing crushed aggregates, than for ellipsoidal aggregates, representing rounded aggregates. An important factor that affected the

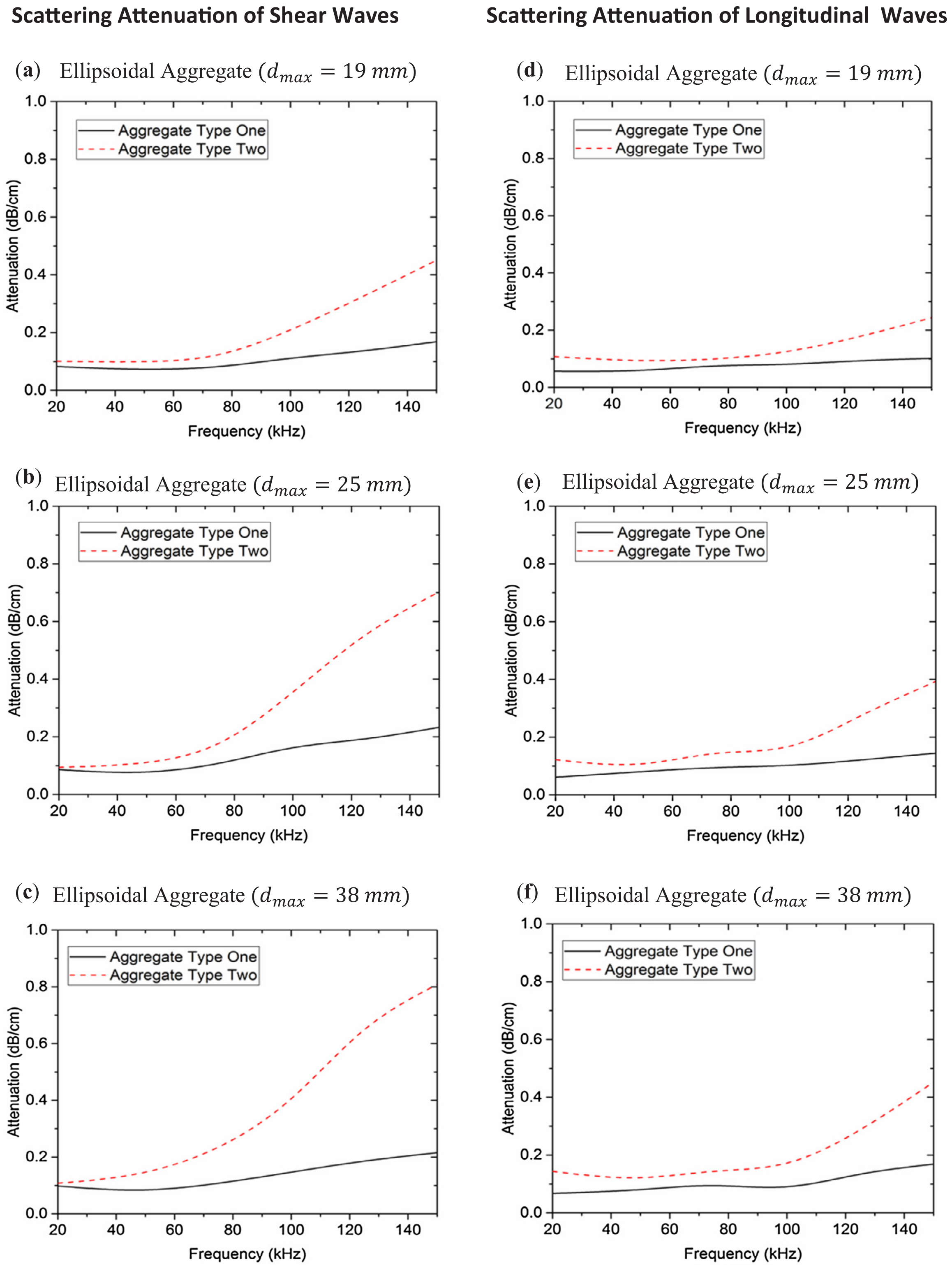

Fig. 11. Scattering attenuation of horizontal shear waves in synthetic concrete specimens with zero air void volume with ellipsoidal aggregates of maximum size of (a) 19mm, (b) 25mm, and (c) 38mm, and scattering attenuation specimens of longitudinal waves in the synthetic concrete specimens with zero air void volume with ellipsoidal aggregates of maximum size of (d) 19mm, (e) 25mm and (f) 38mm.

scattering attenuation was the material properties of aggregates. For aggregates with a large acoustic impedance, the scattering attenuation was significant. The effect of air voids in scattering attenuation was not significant; they slightly affected the scattering attenuation for frequencies higher than about 80 kHz. Generally, the scattering attenuation for emitted signals with the center frequency of 50 kHz and lower was small. Similar behavior was observed for longitudinal waves. However, the scattering attenuation of horizontal shear waves was larger than that of longitudinal waves. As the frequency increased, the difference between the scattering attenuation of shear and longitudinal waves increased as well.

Acknowledgement

We would like to thank the anonymous reviewers since their comments enhanced the quality of this work in many aspects.

References

[1] D.M. McCann, M.C. Forde, Review of NDT methods in the assessment of concrete and masonry structures, Ndt E Int. 34 (2) (2001) 71–84.
[2] T. Planès, E. Larose, A review of ultrasonic Coda Wave Interferometry in concrete, Cem. Concr. Res. 53 (2013) 248–255.
[3] S.K.U. Rehman, Z. Ibrahim, S.A. Memon, M. Jameel, Nondestructive test methods for concrete bridges: a review, Constr. Build. Mater. 107 (2016) 58–86.
[4] F. Schubert, B. Köhler, Ten lectures on impact-echo, J. Nondestr. Eval. 27 (1–3) (2008) 5–21.
[5] O. Aldo, A.A. Samokrutov, P.A. Samokrutov, Assessment of concrete structures using the Mira and Eyecon ultrasonic shear wave devices and the SAFT-C image reconstruction technique, Constr. Build. Mater. 38 (2013) 1276–1291.
[6] K. Hoegh, L. Khazanovich, Extended synthetic aperture focusing technique for ultrasonic imaging of concrete, NDT E Int. 74 (2015) 33–42.
[7] P. Choi, D.H. Kim, B.H. Lee, M.C. Won, Application of ultrasonic shear-wave tomography to identify horizontal crack or delamination in concrete pavement and bridge, Constr. Build. Mater. 121 (2016) 81–91.
[8] J.B. White, K.T. Wieghaus, M.M. Karthik, P. Shokouhi, S. Hurlebaus, A. Wimsatt, Nondestructive testing methods for underwater tunnel linings: practical application at chesapeake channel tunnel, J. Infrastruct. Syst. 23 (3) (2016) B4016011.
[9] K. Freeseman, L. Khazanovich, K. Hoegh, A. Nojavan, A.E. Schultz, S.H. Chao, Nondestructive monitoring of subsurface damage progression in concrete columns damaged by earthquake loading, Eng. Struct. 114 (2016) 148–157.
[10] L. Khazanovich, K. Freeseman, L. Salles, A. Asadollahi, Damage Detection Techniques for Concrete Applications (No. CHPP Report-UMN# 1-2016), Michigan State University. Center for Highway Pavement Preservation, 2016.
[11] M. Grohmann, E. Niederleithinger, S. Buske, Geometry determination of a foundation slab using the ultrasonic echo technique and geophysical migration methods, J. Nondestr. Eval. 35 (1) (2016) 17.
[12] A. Asadollahi, L. Khazanovich, Analytical reverse time migration: an innovation in imaging of infrastructures using ultrasonic shear waves, Ultrasonics 88 (2018) 185–192.
[13] M. Schickert, M. Krause, W. Müller, Ultrasonic imaging of concrete elements using reconstruction by synthetic aperture focusing technique, J. Mater. Civ. Eng. 15 (3) (2003) 235–246.
[14] K. Nakahata, G. Kawamura, T. Yano, S. Hirose, Three-dimensional numerical modeling of ultrasonic wave propagation in concrete and its experimental validation, Constr. Build. Mater. 78 (2015) 217–223.
[15] F. Schubert, B. Köhler, Three-dimensional time domain modeling of ultrasonic wave propagation in concrete in explicit consideration of aggregates and porosity, J. Comput. Acoust. 9 (04) (2001) 1543–1560.
[16] F. Schubert, R. Marklein, Numerical computation of ultrasonic wave propagation in concrete using the elastodynamic finite integration technique (EFIT), Ultrasonics Symposium, 2002. Proceedings. 2002 IEEE, IEEE, 2002, pp. 799–804.
[17] F. Schubert, Numerical time-domain modeling of linear and nonlinear ultrasonic wave propagation using finite integration techniques—theory and applications, Ultrasonics 42 (1–9) (2004) 221–229.
[18] T.P. Philippidis, D.G. Aggelis, Experimental study of wave dispersion and attenuation in concrete, Ultrasonics 43 (7) (2005) 584–595.
[19] P. Fellinger, R. Marklein, K.J. Langenberg, S. Klaholz, Numerical modeling of elastic wave propagation and scattering with EFIT—elastodynamic finite integration technique, Wave Motion 21 (1) (1995) 47–66.
[20] J. Bingham, M. Hinders, Lamb wave characterization of corrosion-thinning in aircraft stringers: experiment and three-dimensional simulation, J. Acoust. Soc. Am. 126 (1) (2009) 103–113.
[21] F. Schubert, A. Peiffer, B. Köhler, T. Sanderson, The elastodynamic finite integration technique for waves in cylindrical geometries, J. Acoust. Soc. Am. 104 (5) (1998) 2604–2614.
[22] F. Collino, C. Tsogka, Application of the perfectly matched absorbing layer model to the linear elastodynamic problem in anisotropic heterogeneous media, Geophysics 66 (1) (2001) 294–307.
[23] D. Komatitsch, J. Tromp, A perfectly matched layer absorbing boundary condition for the second-order seismic wave equation, Geophys. J. Int. 154 (1) (2003) 146–153.
[24] J. Kristek, P. Moczo, M. Galis, A brief summary of some PML formulations and discretizations for the velocity-stress equation of seismic motion, Stud. Geophys. Geod. 53 (4) (2009) 459.
[25] P. Wriggers, S.O. Moftah, Mesoscale models for concrete: homogenisation and damage behaviour, Finite Elements Anal. Des. 42 (7) (2006) 623–636.
[26] L. Liu, D. Shen, H. Chen, W. Xu, Aggregate shape effect on the diffusivity of mortar: a 3D numerical investigation by random packing models of ellipsoidal particles and of convex polyhedral particles, Comput. Struct. 144 (2014) 40–51.
[27] X. Wang, M. Zhang, A.P. Jivkov, Computational technology for analysis of 3D mesostructure effects on damage and failure of concrete, Int. J. Solids Struct. 80 (2016) 310–333.
[28] Z. Qian, E.J. Garboczi, G. Ye, E. Schlangen, Anm: a geometrical model for the composite structure of mortar and concrete using real-shape particles, Mater. Struct. 49 (1–2) (2016) 149–158.
[29] L. Godinho, D. Dias-da-Costa, P. Areias, E. Júlio, D. Soares Jr, Numerical study towards the use of a SH wave ultrasonic-based strategy for crack detection in concrete structures, Eng. Struct. 49 (2013) 782–791.
[30] G.K. Kocur, E.H. Saenger, T. Vogel, Elastic wave propagation in a segmented X-ray computed tomography model of a concrete specimen, Constr. Build. Mater. 24 (12) (2010) 2393–2400.